Journal of Wind Engineering & Industrial Aerodynamics 184 (2019) 49–60

Contents lists available at ScienceDirect

Journal of Wind Engineering & Industrial Aerodynamics

journal homepage: www.elsevier.com/locate/jweia

Aerodynamic characteristics of generic ice shells

Arash Raeesi *, Sean McTavish, Annick D'Auteuil

National Research Council Canada, Ottawa, Canada

ARTICLE INFO

Keywords:
Bridge cable
Ice accretion
Ice fragment
Ice trajectory model
Ice shell aerodynamics
Wind tunnel

ABSTRACT

Freezing rain and wet snow can cause ice to accumulate on the surface of bridge cables. Subsequently, a rise in temperature and wind can cause ice to shed from the surface of cables. Several instances of ice and wet snow shedding from bridge cables have been observed in Canada. Environmental predictive models have been proposed to predict the ice shedding behaviour and its trajectory from bridge cables. The current study aims at measuring the aerodynamic force and moment coefficients of generic ice fragments detached from a bridge cable as a priori for a subsequent ice trajectory model. Nine representative generic, ice shells were selected to represent different aspect ratios, curvatures, ice thicknesses, and external ice surface conditions. Aerodynamic forces and moments were measured for each of the ice shell models in turbulent flow for a wide range of orientations. The use of a curved shape as opposed to a flat plate resulted in a significant difference in the aerodynamic coefficients. It was found that the aspect ratio was the most important geometric factor in determining the aerodynamic forces and moments on the curved models. The findings of this study will be implemented in future ice trajectory models.

1. Introduction

Snow and ice can accrete on the high-density polyethylene (HDPE) sleeve of the stay cables of cable-stayed bridges. As the ice and snow accumulates and melts, large fragments of ice or snow can be shed from the cables and represent a potential safety risk to bridge users. For example, the Port Mann cable-stayed bridge in Vancouver, Canada was opened to traffic in 2011, and during its first year of service, ice and wet snow built up on the stay cables and ice/snow pieces fell onto the traffic lanes leading to damage to multiple vehicles, injuries to pedestrians and closure of the bridge for multiple hours (Ng, 2012; Canadian Consulting Engineer, 2013). More recently, in December 2016, a similar situation occurred on the same bridge. The Pierre- Laporte bridge in Québec City, Canada was closed in February 2018 because pieces of ice fell from the main cables of this suspension bridge (Neron, 2017). Such events are expected to become more frequent due to the effects of climate change (Cheng et al., 2007, 2011).

The trajectory of an ice fragment shed from an inclined cable such as a stay cable or a suspension bridge cable will depend on the wind direction, wind speed, and the shape of the fragment. The shape of an ice fragment will affect its aerodynamic forces and moments, which will cause certain fragments to fall closer to the vertical plane of inclined cables, while others may be carried further downstream by the wind. The majority of the trajectory models available in literature have been developed to study the behaviour of spherical, rod-like, or plate-like wind-borne debris, such as rocks, beams, or plywood, that would result from an extreme wind storm. Early trajectory models represented the debris trajectory as a 2 degree-of-freedom (DOF) system where the particle is subjected to a drag force and gravity (Holmes, 2004). The trajectory models applied by Biswas et al. (2012), and Renström (2015) evaluated ice thrown from a rotating wind turbine blade. These two models added the lift force to the equations of motion, but focused predominantly on compact, cube-shaped debris that was subjected to a drag force and gravity. Other trajectory models by Holmes et al. (2006) and Baker (2007) added the effect of the lift force and pitching moment to the equations of motion and included lift and drag forces resulting from wind tunnel tests on flat plates. Holmes et al. (2006) demonstrated that the rotation induced lift through the Magnus effect and had a significant influence on the trajectory of flat plates.

A more generalized, 6-DOF model for the trajectory of flat plates was developed by Richards et al. (2008) and was based on forces and moments acquired during a wind tunnel test on plates and rods (Richards, 2010). This model has formed the basis for the subsequent trajectory models of Martinez-Vazquez et al. (2009), Noda and Nagao (2010), Grayson et al. (2012), and Fu et al. (2013). One of the limitations in extending existing trajectory models to ice fragments shed from an inclined bridge cable is that the models are based on force and moment data for flat plates. Ice fragments that fall from inclined cables typically

* Corresponding author.
E-mail address: arash.raeesi@nrc-cnrc.gc.ca (A. Raeesi).

https://doi.org/10.1016/j.jweia.2018.11.002
Received 12 July 2018; Received in revised form 24 October 2018; Accepted 3 November 2018

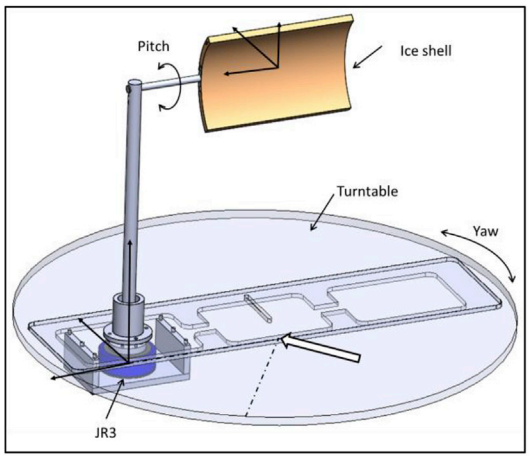

(a) Isometric view. looking upstream.

(b) Setup in the tunnel showing the S9-Sim model,

Fig. 1. Support structure and experimental setup in the NRC 1.0 m × 0.8 m Pilot Wind Tunnel.

have a shape that resembles a cylindrical arc, which has some characteristics of a cambered airfoil (Szilder, 2017, 2018). Additionally, the forces and moments generated by a falling ice shells will be a function of factors such as the aspect ratio of the shells, the radius of the cable, and the type of ice that has formed on the stay cable.

A wind tunnel test was conducted in the NRC 1.0 m × 0.8 m Pilot Wind Tunnel to evaluate the forces acting on several pre-defined, generic ice shells. The ice shell models were printed using Selective Laser Sintering (SLS) with parametric variations in aspect ratio, curvature, and thickness. The measurement database generated the force and moment coefficients that are required by a 6-DOF numerical model to predict the trajectory of falling ice fragments. The results obtained from this study will provide appropriate data leading to improved environmental prediction models that will result in safer bridge operations.

2. Experimental setup

The experiment was conducted in the NRC 1.0 × 0 0.8 m Pilot Wind Tunnel in January 2018. This wind tunnel can be operated with either a 3/4-open jet or a closed test section. The closed test section was used for this study. The wind tunnel has a height of 0.8 m, a width of 1 m, and a maximum speed of 44 m/s in a closed, empty test section.

The experimental setup shown in Fig. 1 consisted of a vertical support arm and a horizontal support arm which positioned the centre of each model at the centre of the test section. The vertical support arm had a length of 40 cm. The vertical support arm was shielded from the wind using a concentric tube that was fastened to a flange located at the turntable surface. This shroud is not shown in the rendering in Fig. 1a, but can be seen in Fig. 1b. Three different horizontal support arms were used with lengths that ranged from 10.2 cm to 15.6 cm depending on the width of the ice shell in the tunnel. The horizontal support arms were matched with the ice shells such that the model was always located at the centre of the test section. The experimental setup had two degrees of freedom. The model could be adjusted manually in pitch and could be adjusted in yaw using the automated turntable (Fig. 1a).

Experiments were conducted in turbulent flow for all of the ice shells and in smooth flow for a subset of the models to evaluate the effect of turbulence on the forces and moments. Turbulence bars were fabricated for the experiment. The turbulence bars had a height of 0.8 m, a square cross-section of 8 mm × 8 mm, and a centre-to-centre spacing of 50 mm. The grid was located 0.614 m upstream of the centre of the turntable. At this position, the boundary layer height is less than 100 mm from the floor and ceiling, the velocity and turbulence intensity profiles outside of the boundary layer are uniform, the longitudinal turbulence intensity in

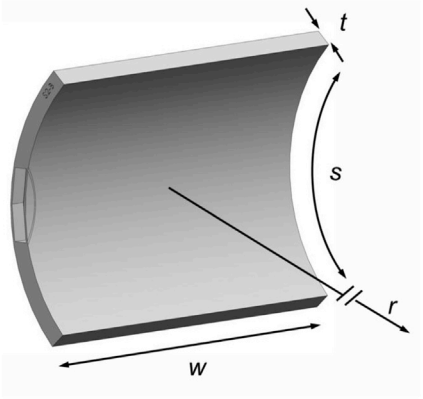

(a) Schematic of a generic ice shell with characteristic parameters.

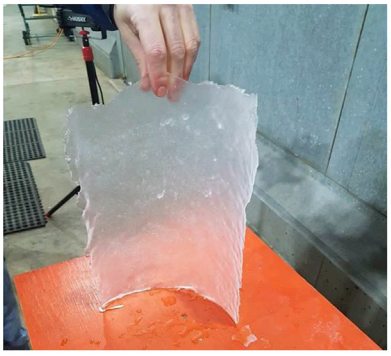

(b) Ice shell detached from a cable model in the NRC Climatic Testing Facility.

Fig. 2. Definition of generic ice shells; Top: rendering with characteristic parameters, Bottom: photograph of ice piece detached from a stay cable model in NRC climatic test facility.

the freestream is 7%, and the length scale at the centre of the test section is approximately 5 cm. While the length scales are smaller than what would be expected at a bridge site, the turbulence intensity is representative of the conditions in the field. The turbulence bars used in the experiment can be seen upstream of a model in Fig. 1b. A thin helical wire (24 American wire gauge) was wrapped around the turbulence bars to mitigate the generation of a high-pitched sound emitted by the bars near the desired wind speed set point. The turbulence intensity in smooth flow is nominally 1%–1.5% in the vicinity of the model. The wind speed in the

Table 1
Dimensions of the ice shells.

Model	arc length (s) [cm]	width (w) [cm]	thickness (t) [cm]	radius (r) [cm]	AR (w/s) [-]
S1-V	11.25	22.5	1	–	2
S2-B	15	22.5	1	10	1.5
S3-AR-2	11.25	22.5	1	10	2
S4-AR-0.5	22.5	11.25	1	10	0.5
S5-AR-1	15	15	1	10	1
S6-t1.5	15	22.5	1.5	10	1.5
S7-C8	15	22.5	1	8	1.5
S8-C15	15	22.5	1	15	1.5
S9-Sim	15	22.5	1	10	1.5

test section was calibrated prior to conducting the experiment using a Pitot-static probe mounted at the centre of the test section in smooth flow and in turbulent flow.

Forces were measured using a six-component fast-response balance (JR3, Model 30E12A4-U562-EF). As shown in Fig. 1a, the balance was located under the floor of the test section. The base plate of the balance was fastened to the underside of the turntable and, therefore, the balance rotated with the model. The balance voltages were low-pass filtered at a frequency of 42 Hz. Signals were acquired by a National Instruments PCI-6225 data acquisition system at a frequency of 100 Hz and with a sampling time of 15 s.

The use of an unshielded horizontal support strut meant that the balance sensed the forces and moments acting on the model in addition to those acting on the horizontal strut. A secondary setup was therefore designed to characterize the forces on the support strut in the presence of the model. The strut-tare setup will be described in greater detail in Section 2.4.

2.1. Ice shells

Several generic ice shells were considered to evaluate the aerodynamic forces and moments acting on representative ice fragments that could detach and fall from a bridge cable. The ice shell models were partial cylindrical shells with an inner radius that would match the radius of a bridge cable (geometric scale of 1:1). The shells were 3D printed using SLS and were mounted onto an insert located at the end of the horizontal support arm. A schematic of the geometrical parameters of the studied representative ice shells is shown in Fig. 2a. The geometrical parameters of ice shells that were varied included the arc length (s), the width of the shell (w), the thickness (t), the inner radius (r), and the aspect ratio ($AR = w/s$). The ice shells and their dimensions are described in Table 1. For the reader's better perspective, a sample ice fragment that could detach from a stay cable can be seen in Fig. 2b. This photo is the courtesy of a separate study conducted at the NRC Climatic Testing Facility.

Nine ice shells were developed and were named for their primary feature. Model S1-V was a flat plate that was used for validation with available data in literature. The baseline ice shell model, S2-B, had a radius of 10 cm (corresponding to a bridge cable of 20 cm diameter), an arc length of 15 cm, a width of 22.5 cm, and a thickness of 1 cm. The 1 cm ice shell thickness was selected based on 10 mm of ice accumulation on a bridge cable, which could result from 25 mm of vertical freezing rain precipitation. It should be noted that 25 mm of freezing rain precipitation has a return period of well below 50 years in eastern Canada and in the northeastern United States (Structural Engineering Institute, 2010; Canadian Standards Association, 2010). Models S3-AR-2, S4-AR-0.5, and S5-AR-1 varied the aspect ratio (AR) of the ice shells whereas Model S6-t1.5 had a thickness (t) that was increased by 50% relative to the baseline shape. Models S7-C8 and S8-C15 had respective inner radii of 8 cm and 15 cm, representing ice that would form on stay cables with

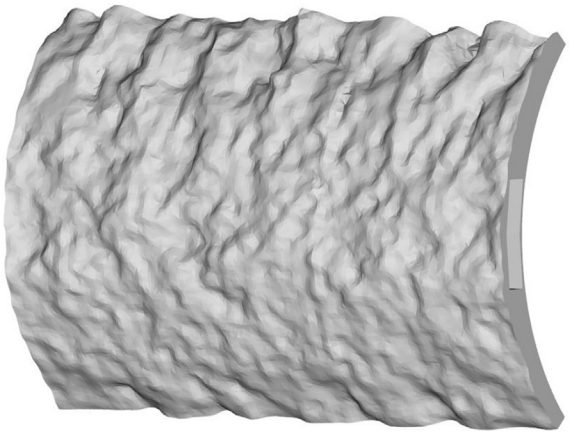

(a) Computational model of S9-Sim.

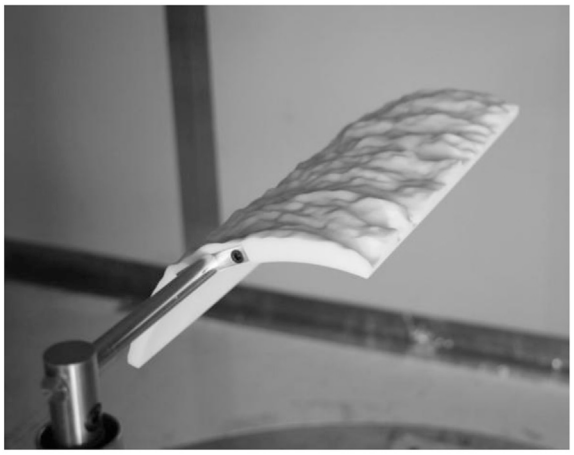

(b) Model S9-Sim installed in the wind tunnel.

Fig. 3. Ice shell S9-Sim with simulated surface texture.

diameters of 16 cm and 30 cm. Models S1-V to S8-C15 had smooth inner and outer surfaces that resulted from the SLS fabrication process. It was also desired to evaluate the characteristics of a representative ice shells with a textured surface as compared to the aerodynamic characteristics of the generic smooth ice shells. As a result, the surface of last model, S9-Sim, was generated based on numerical simulations of freezing rain accretion on a stay cable conducted using the NRCs morphogenetic ice accretion code (Szilder, 2017, 2018). The computations were carried out assuming a cable inclined at 60°, a wind direction 225° from the main cable axis (where 0° corresponds to the flow aligned with the vertical cable plane and moving downward along the cable), a wind speed of 6 m/s, an air temperature of -5°, 10 h of precipitation at a rate of 2.5 mm/h, and a cable surface with a double-parallel helical fillet. The surface texture of the ice accumulation generated by the simulations was printed with the same aspect ratio and radius of curvature as the baseline model, S2-B. This allowed the effect of a realistic ice surface (Model S9-Sim) to be compared to a smooth-surfaced, generic, ice shell (Model S2-B). Model S9-Sim has a smooth inner surface as this represents the surface that touches the stay cable. A rendering and a photograph of the simulated model (S9-Sim) are shown in Fig. 3.

2.2. Test program

The test plan summarized in Table 2 consisted of a series of yaw

Table 2
Summary of the test program.

Model	Variation of	Turbulent Baseline shape	Smooth	Yaw Sweeps	Re-Sweeps	Horizontal arm measurements [cm]	Strut-tare data applied	Strut-tare
S1-V	flat plate for Validation (V)	•		•		10.2		A
S2-B	NA	•	•	•	•	10.2	A	A
S3-AR-2	Aspect Ratio (AR)	•		•		10.2		A
S4-AR-0.5	Aspect Ratio (AR)	•		•		15.6	B	B
S5-AR-1	Aspect Ratio (AR)	•		•		13.8	C	C
S6-t1.5	Thickness (t)	•		•		10.2		A
S7-C8	Curvature (C)	•		•		10.2		A
S8-C15	Curvature (C)	•		•		10.2		A
S9-Sim	Surface (Sim)	•	•	•	•	10.2	A	

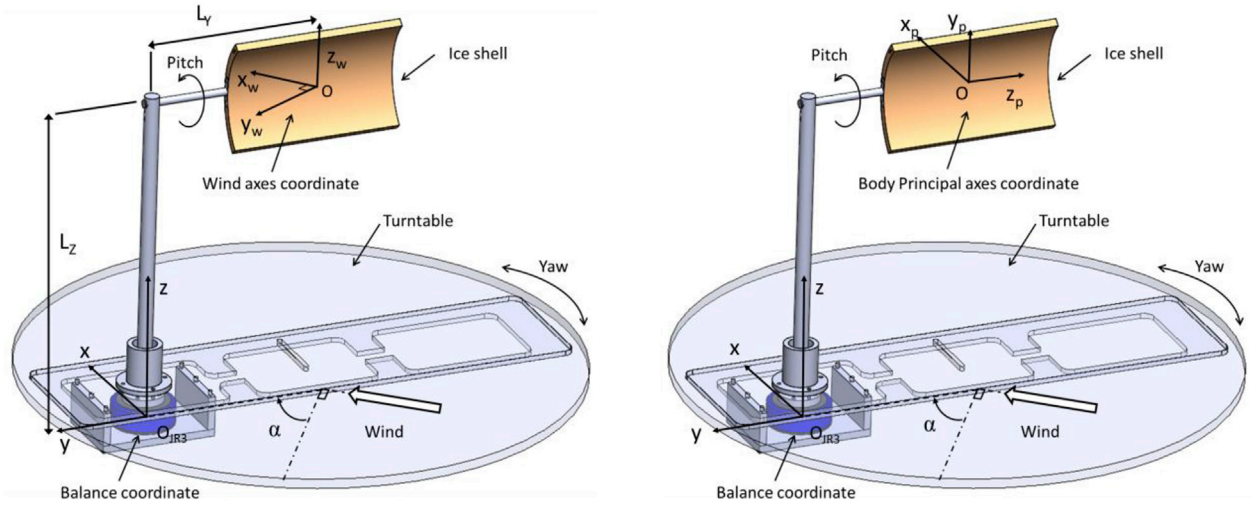

(a) Balance and wind axis coordinate system. system.

(b) Balance and body principal axis coordinate

Fig. 4. Description of the coordinate systems.

sweeps (α) for a given pitch angle (θ). Each ice shell model was first placed at θ = 0° and data were acquired at discrete yaw angles (α) ranging from 0° to +180°, based on the angle convention shown in Fig. 4. After each yaw sweep was conducted, the pitch angle of the ice shell was increased manually by 10° and the next yaw sweep was conducted. This process was repeated for pitch angles ranging from 0° to 90°. In addition to these yaw sweeps, Reynolds number sweeps were conducted with models S2-B and S9-Sim. All of the ice shells were tested in turbulent flow, and models S2-B and S9-Sim were also evaluated in smooth flow. The tests were conducted with a wind speed of 14 m/s when the pitch angle of the model was less than 60°. However, at high pitch angles (θ > 60°), the wind speed had to be reduced to approximately 11–12 m/s to prevent the models from vibrating. The insensitivity of the force and moment coefficients to changes in the Reynolds number over this range of wind speeds will be discussed below in Section 3.3.

2.3. Coordinate system definitions

The relative orientation of the ice shells in the wind tunnel is described by the yaw angle (α) and the pitch angle (θ). These two angles are defined in Fig. 4a. A positive yaw angle corresponds to a clockwise rotation of the turntable when viewed from above. A 0° yaw angle occurs when the ice-piece model is facing directly into the wind with the wind pointing toward the concave surface of the model. The pitch angle θ is varied by manually rotating the model around the horizontal strut counter-clockwise as shown in Fig. 4a. The case shown in Fig. 4a refers to a 90° pitch angle and therefore 0° pitch corresponds to the case where the convex surface of the model is pointing upward.

The output from the balance is in the balance coordinate system which is located at the geometrical centre of the sensor as shown in Fig. 4a and b. The balance was mounted underneath the turntable and rotated with the turntable. When the yaw angle was 0°, the X-Axis of the balance coincided with the wind direction and the Y-Axis of the balance was in the horizontal plane and was positive toward the starboard direction. The Z-Axis of the balance was in the vertical direction. The wind axis coordinate system is a fixed coordinate system located at the centre of turntable at a height corresponding to the centre of the model. The XW -Axis is parallel to the flow direction, the YW -Axis is toward the starboard side of the model and the ZW -Axis is vertical and positive upwards as shown in Fig. 4a. The forces were also transformed into a body-aligned principal axis coordinate system for use with a 6-DOF trajectory model. The body principal axis is defined as a moving coordinate system which is always attached to the model as shown in Fig. 4b and located at its geometrical centre. The XP-Axis is always normal to the model and points toward the concave side of the ice shell, whereas the ZP-Axis is along the length of the model and the YP-Axis is normal to both XP and ZP. For a yaw angle of α = 0° and a pitch angle of θ = 90°, the body principal axis coincides with the wind axis coordinate system.

2.4. Correction for strut effects

To account for the aerodynamic loads acting on the top of the vertical

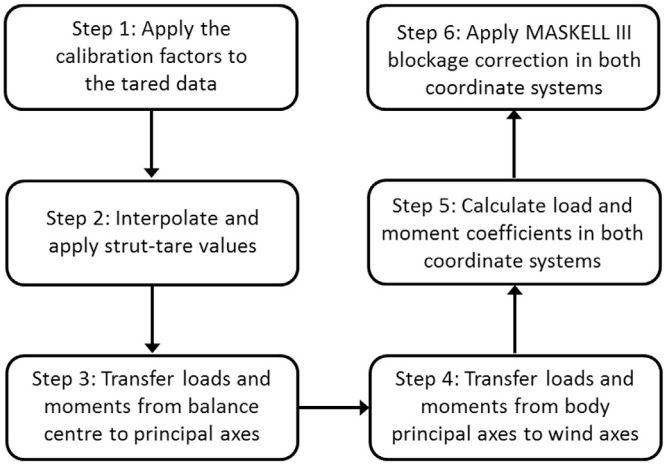

Fig. 5. Data reduction process.

post and on the horizontal strut, a series of strut-tare tests were conducted as summarized in Table 2. Strut-tare tests were conducted for the three horizontal arm lengths. During the strut-tare tests, the model was supported separately using a second vertical post attached to the centre of the turntable to replicate similar aerodynamic behaviour, and a small gap was maintained between the model and the horizontal strut. Strut-tare yaw sweeps were conducted for a particular ice shell at pitch angles of 0°, 30°, 60°, and 90°. The resulting force coefficients were interpolated for other pitch angles. The strut-tare results for a given arm length were then applied to other ice shells that used the same horizontal arm. For instance, the strut-tare forces and moments were obtained for the 10 cm horizontal arm using Shape S2-B (Setup A in Table 2). The strut-tare values were then applied for all other ice shell models that had the same horizontal arm length. There may be some differences in the effect of the flow around the ice shell on the strut between the various ice shells using the 10 cm horizontal arm, but these were assumed to be minor compared to the effect of pitch angle and the horizontal arm length. It should be noted that in this setup, the models had to be supported from underneath and only pitch angles between 90° and 180° could be achieved. This arrangement of the model would therefore correspond to inverted flow patterns from those in regular tests near the model. It was assumed that since the ice shell in the strut-tare setup was a mirror image of its orientation in the regular tests, the flow patterns would also be mirrored, and the appropriate force components in the balance axis were reversed in the strut-tare tests before applying the tare values in the data reduction process.

2.5. Data reduction steps

Data reduction was applied to the tared balance forces and moments. A block diagram of the data reduction steps is shown in Fig. 5. The first data reduction step was to apply the calibration factors to the force and moment voltages from the balance. The second step of the data reduction process was to apply the strut-tare values. The setup strut-tare tests were conducted for all yaw angles and a limited combination of pitch angles. The strut-tare values were then interpolated for the entire pitch angle range. The force and moment values were corrected by subtracting the corresponding strut-tare values (for each strut arm length, yaw, and pitch angle combination) from the balance forces and moments. The third data reduction step was to transfer the forces/moments from the balance centre to the body principal axis and wind axis coordinate systems described in Fig. 4. The aerodynamic force and moment coefficients were calculated after the engineering values were transformed to the wind and principal axis coordinate systems. The Maskell III blockage correction was then applied to the force and moment coefficients in both coordinate systems. The maximum geometric blockage was 4.2% based on the

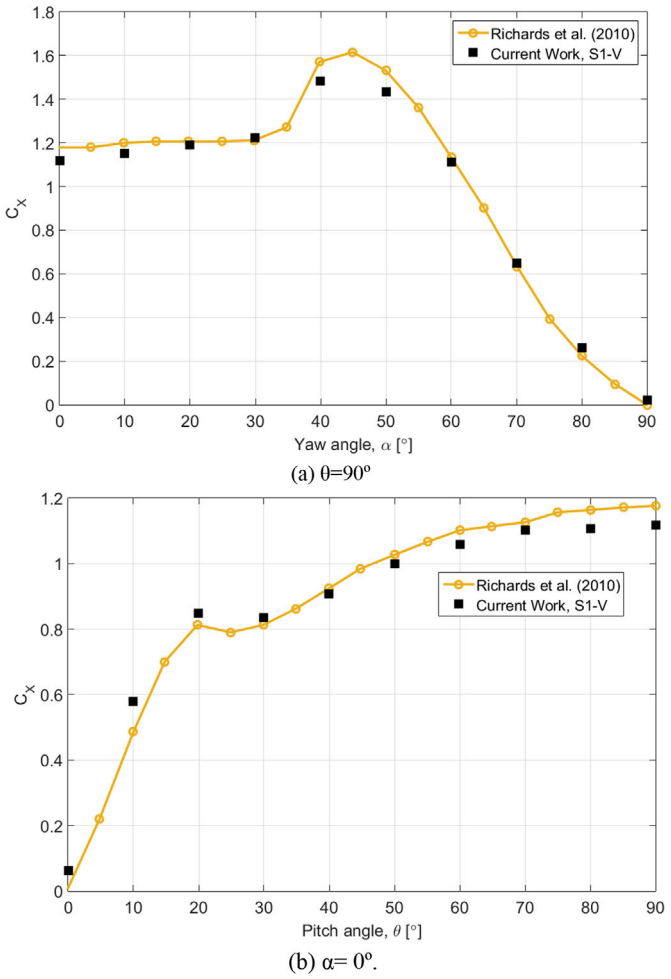

Fig. 6. Validation of normal force coefficient C_X results with Richards (2010) with respect to yaw angle (top) and pitch angle (bottom).

frontal area of an ice-piece and the cross-sectional area of the wind tunnel.

In the wind axis coordinate system, the blockage-corrected drag (C_D), side (C_S), and lift (C_L) force coefficients are defined as:

$$\begin{bmatrix} C_D \\ C_S \\ C_L \end{bmatrix} = \frac{1}{1/2\rho U^2 ws} \begin{bmatrix} F_{XW} \\ F_{YW} \\ F_{ZW} \end{bmatrix} \quad (1)$$

where F represents the forces in the wind axis coordinate system, ρ is the air density, U is the blockage-corrected wind speed and w and s are respectively the width and the arc length of the model from Table 1. Similarly, the roll (C_{ROLL}), pitch (C_{PITCH}), and yaw (C_{YAW}) moment (M) coefficients are calculated as:

$$\begin{bmatrix} C_{ROLL} \\ C_{PITCH} \\ C_{YAW} \end{bmatrix} = \frac{1}{1/2\rho U^2 ws} \begin{bmatrix} M_{XW} \\ M_{YW} \\ M_{ZW} \end{bmatrix} \quad (2)$$

3. Results

The force and moment coefficients in the wind axis coordinate system were calculated according to Equations (1) and (2). The coefficients in the body principal axis coordinate system were calculated for the development of a 6-DOF ice particle trajectory model and used reference lengths for normalization that are consistent with those shown in Equations (1) and (2). However, with the exception of the validation results, the results in this article will be presented in the wind axis system. The results of the

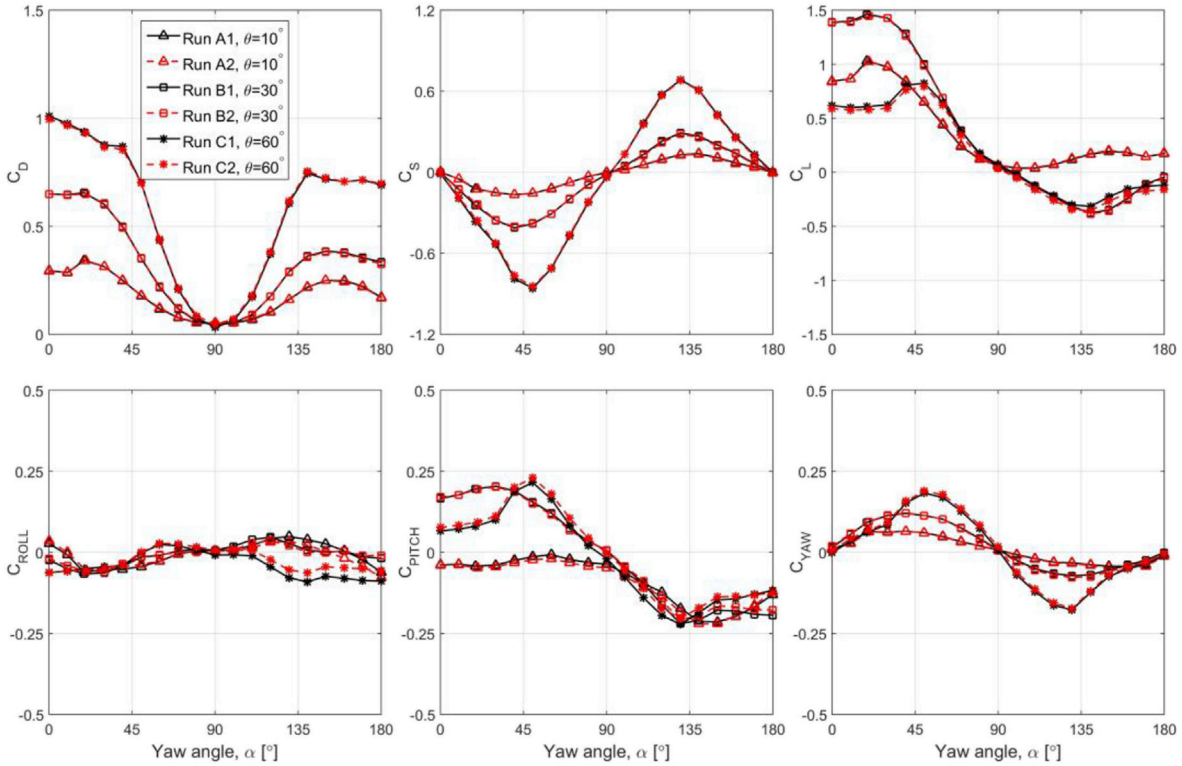

Fig. 7. Repeatability of Model S2-B results in turbulent flow. From top left: drag force coefficient, side force coefficient, lift force coefficient, rolling moment coefficient, pitching moment coefficient, and yawing moment coefficient.

parametric study on the forces and moments of the ice shells will be demonstrated below using a subset of the pitch angles that were evaluated.

3.1. Validation of results

The normal force coefficient results (C_X in the principal axes) for the flat plate shape were validated using data from Richards (2010), as shown in Fig. 6. The flat plate model from Richards (2010) had an aspect ratio of 2, a t/s ratio of 0.02 (based on the geometrical definitions in the current paper), and data were acquired in smooth flow at a Reynolds number of approximately 1.7105. The current results for Model S1-V had an aspect ratio of 2, a t/s ratio of 0.09, and were acquired in turbulent flow (7% turbulence intensity, 0.05 m length scale) at a Reynolds number of approximately 1×10^5. In Fig. 6a, the normal force coefficients from both studies are plotted against the yaw angle at a fixed pitch angle of $\theta = 90°$. In this case, the maximum difference between the results of the two studies is approximately 6% at $\alpha = 50°$. In Fig. 6b, the normal force coefficients from both studies are plotted against θ at a yaw angle of $\alpha = 0°$. The maximum difference between the two studies in Fig. 6b is at $\theta = 0°$ where in the current study $C_X = 0.062$ and in Richards (2010) $C_X = 0.005$. Overall, a good level of agreement can be seen between the results of the present study and those of Richards (2010).

3.2. Repeatability

A number of tests for Model S2-B for pitch angles of 0°, 30°, and 60° were repeated following several model changes over a two day period to evaluate the repeatability of the setup. The results for all of the force and moment coefficients in the wind axes are presented in Fig. 7. It can be seen that the results show good repeatability of the measurement technique. For example, the maximum lift coefficient at $\theta = 30°$ has a percent difference of 1% between the two tests. The largest errors in repeatability were at $\theta = 60°$, where the percent difference in the lift coefficient between the two tests was 5% near the maximum lift coefficient.

3.3. Reynolds number effect

Most of the tests in the current work were conducted at a wind speed of approximately 14 m/s. The Reynolds number was defined based on the blockage-corrected wind speed, the density, the dynamic viscosity (μ), and the arc length of the ice-pieces:

$$Re = \frac{\rho U s}{\mu} \tag{3}$$

For Model S2-B, a wind speed of 14 m/s corresponds to a Reynolds number of approximately $1.4\ 10^5$. Several Reynolds number sweeps were conducted for models S2-B and S9-Sim in both turbulent flow and smooth flow to evaluate the Reynolds insensitivity of the ice shells, as shown in Fig. 8. Except for small variations in the lift coefficient, the coefficients are Reynolds number insensitive for Reynolds numbers greater than 1.1×10^5 in turbulent flow. The lift and drag coefficients in smooth flow show a greater level of Reynolds number dependence. This is observed for Model S2-B at $\theta = 0°$ in Fig. 8a and for Model S9-Sim at $\theta = 30°$ in Fig. 8b. The wind speed had to be reduced to between 11 and 12 m/s at high pitch angles ($\theta > 60°$) to prevent the models from vibrating. The drag and lift coefficients are shown to be insensitive to Reynolds number at $\theta = 60°$ in Fig. 8 (likely due to a fixed separation point along the leading edge of the shells at a high pitch angle) and so this adjustment in wind speed is assumed to have a negligible impact on the coefficients.

3.4. Comparison between a flat plate and a curved ice shells

It can be seen from Fig. 9 that the force and moment coefficients for Model S3-AR-2 (particularly the lift and the drag) are distinctively different than those for a flat plate of the same aspect ratio. For instance, at $\theta = 30°$ the magnitude of the lift coefficient of Model S3-AR-2 is approximately 30% larger than that of the flat plate. There is a relatively small, yet significant difference in drag and pitching moment of the two models when placed at a pitch angle of $\theta = 90°$ (i.e. flow is toward the concave surface of

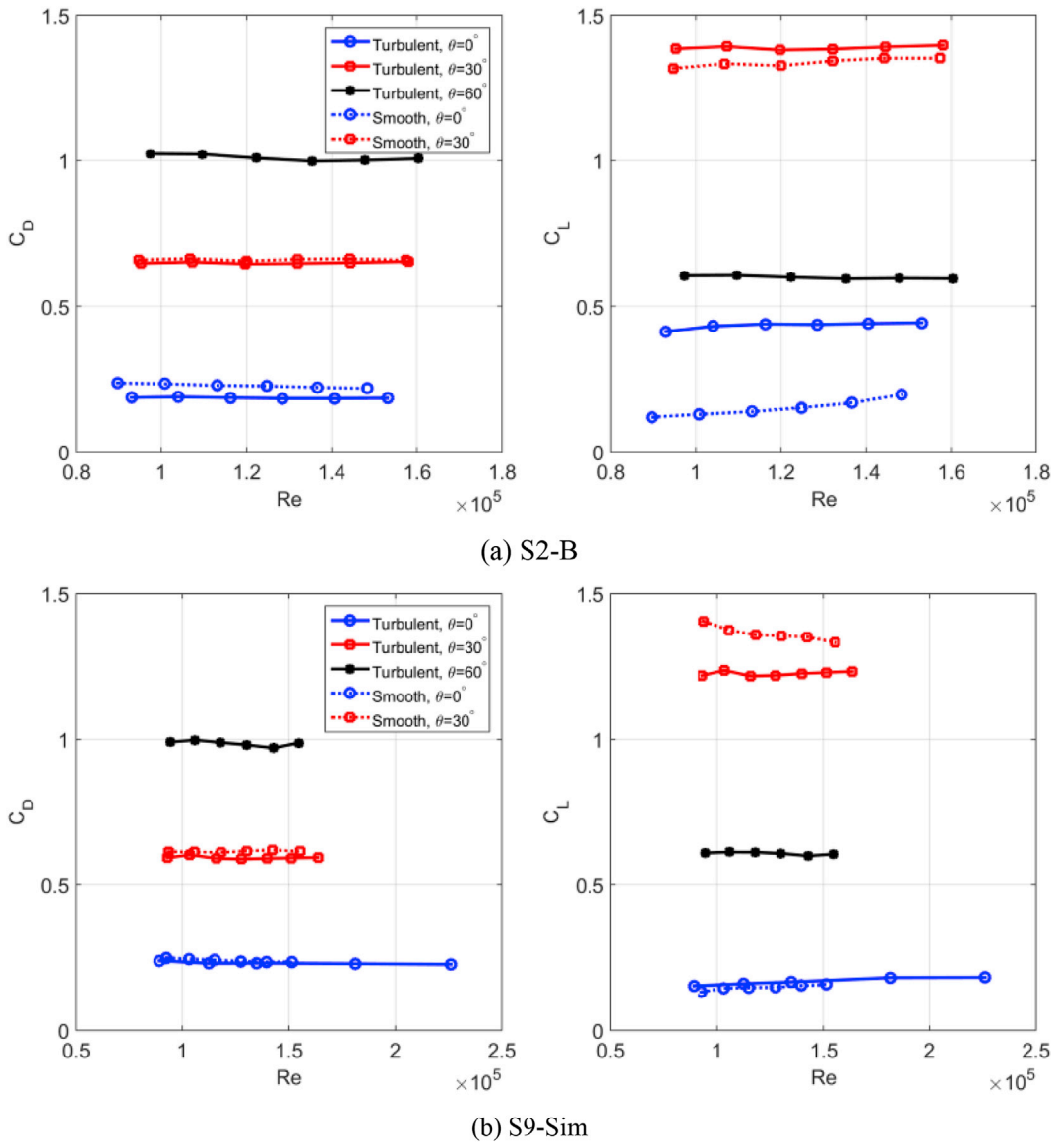

Fig. 8. Reynolds number independence study. a) S2-B model; b) S9-Sim model; Left subfigure: drag force coefficient, Right subfigure: lift force coefficient.

the curved ice shells when $\alpha = 0°$). These results indicate the importance of using these realistic ice shells for ice trajectory prediction software since the aerodynamic forces and moments are one of the important factors for determining the trajectory of a falling ice fragment.

3.5. Effect of aspect ratio

Models S4-AR-0.5, S5-AR-1, S2-B, and S3-AR-2 had a width-to-arc-length aspect ratio of 0.5, 1, 1.5, and 2, respectively, while having the same inner radius of 10 cm. The effect of the aspect ratio on the aerodynamic force and moment coefficients is shown in Fig. 10a, b, and 10c for pitch angles of 10°, 30°, and 90°, respectively. At $\theta = 10°$, the low aspect ratio model (S4-AR-0.5) had the highest C_D, the lowest C_L, and the lowest pitching moment for yaw angles that are less than 60°. At a pitch angle of 30°, the lift and pitching moment coefficients have a larger variation with aspect ratio than the coefficients at 10°. A larger aspect ratio generally resulted in larger lift and pitching moment coefficients for $\theta = 30°$. For instance, in Fig. 10b, the lift coefficient for the low aspect ratio model is about 40% lower than the larger aspect ratios of 1, 1.5, and 2 for yaw angles between 20° and 40°. This difference is even more significant for the pitching moment at yaw angles between 20° and 40° where the sign of the pitching moment switches from the low aspect ratio model (S4-AR-0.5) to the higher aspect ratio models.

For the pitch angle of $\theta = 90°$, the variation of the drag coefficient and the pitching moment are sensitive to the aspect ratio. For instance, the drag coefficient at $\theta = 90°$ increases by more than 30% from the lowest aspect ratio of 0.5 to the highest aspect ratio of 2 as can be seen from Fig. 10c. Although not shown in Fig. 10, the range of variation in the side force coefficient and yawing moment coefficient becomes larger at $\theta = 90°$ compared to the data at $\theta = 30°$. This is likely due to the variation in the flowfield and wake caused by the separation from the vertical edges when $\theta = 90°$ as the aspect ratio is reduced.

3.6. Effect of curvature

The effect of ice shell curvature on C_D and C_L is shown in Fig. 11 for pitch angles of $\theta = 0°$, 10°, and 30°. Models S7-C8, S2-B, and S8-C15 had inner radii of 8.0 cm, 10.0 cm, and 15.0 cm, respectively, while all having an aspect ratio of 1.5. According to the results presented in Fig. 11, the sensitivity of the aerodynamic forces to curvature is generally smaller than the variation in the coefficients that had been observed as a function of aspect ratio (shown earlier in Fig. 10). The drag and lift were the

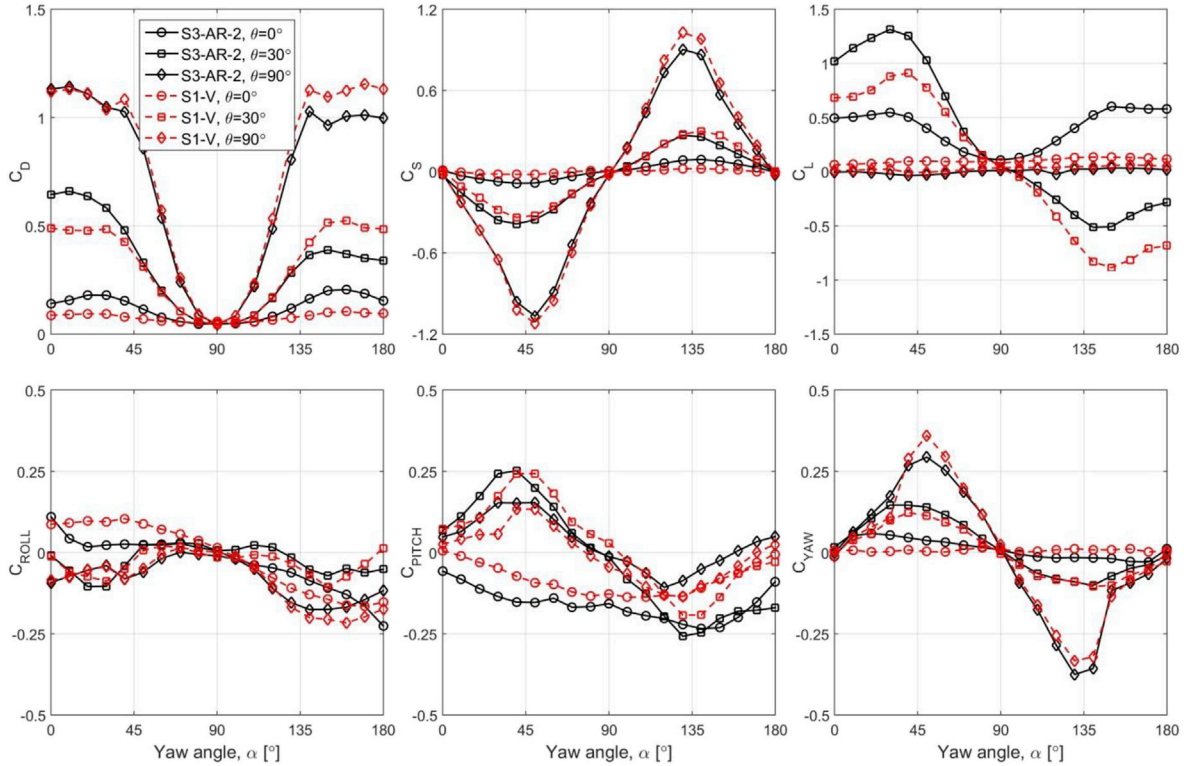

Fig. 9. Comparison of S2-B and S1-V models in turbulent flow. Both models have an aspect ratio of 2. From top left: drag force coefficient, side force coefficient, lift force coefficient, rolling moment coefficient, pitching moment coefficient, and yawing moment coefficient.

coefficients that were the most sensitive to changes in the model curvature. The drag coefficient is typically larger for a lower radius (S7-C8), particularly at small yaw angles ($\alpha < 45°$) and at large yaw angles ($\alpha < 135°$). A possible explanation for this variation is that the separation point shifts toward an upstream location for the lower radius models, leading to larger drag coefficient. For instance, the drag coefficient for Model S7-C8 is about 18% larger than for Shape S8-C15 at yaw angles between $\alpha = 150°$ and $\alpha = 180°$. Similarly, the variation in the lift coefficient is most significant between $\alpha = 0°$ and $\alpha = 40°$, and again between $\alpha = 135°$ and $\alpha = 180°$, where the separation location will be influenced by the curvature of the shell. In the high yaw angle range, the absolute value of the lift coefficient is larger for the larger radius model. For example, when $\theta = 30°$ and $\alpha = 180°$ the lift coefficient for S7-C8 is close to zero ($C_L = -0.026$) whereas the larger radius model, S8-C15, has a lift coefficient of $C_L = -0.31$.

3.7. Effect of ice thickness

Models S2-B and S6-t1.5 had thicknesses of 1.0 cm and 1.5 cm, respectively. It can be seen from Fig. 12 that the 50% increase in thickness for Model S6-t1.5 did not have a significant impact on the drag and lift coefficients. For instance, there is an approximately 7% difference between drag coefficients of S2-B and S6-t1.5 at $\theta = 90°$ and $\alpha = 10°$. A small difference was observed in the rolling moment coefficient of the two ice shells at $\theta = 90°$, between yaw angles of 10° and 50° (not shown). However, since the overall value of the rolling moment was low, it is expected that this will not have a major impact on the moments experience by falling ice fragments.

3.8. Effect of the outer ice surface

Models S2-B and S9-Sim had the same width, arc length, and radius with the only difference being the texture of the outer surface. The outer surface of Model S9-Sim is a numerically-simulated ice surface that represents a more realistic ice shell that could detach from a stay cable, while Model S2-B has a smooth outer surface. The effect of the outer ice surface can be seen in Fig. 13, where C_D and C_L of the two ice-pieces are compared at four pitch angles of 0°, 10°, 30°, and 60°. The effect of the outer surface, especially for the lift coefficient and pitching moment (not shown), was more pronounced at $\theta = 30°$. The maximum lift coefficient associated with the smooth outer surface on Model S2-B was approximately 20%–40% larger than the maximum lift generated by the rougher ice shell model, S9-Sim, at $\theta = 10°$ and $\theta = 30°$. At larger pitch angles, the outer surface has significantly less impact on the aerodynamic forces and moments since the separation location is dictated more by the sharp leading edges of the models and the dimensions of the ice shell, rather than the outer surface texture.

3.9. Effect of turbulence

Tests were conducted in both turbulent and smooth flow for models S2-B and S9-Sim. Reynolds number sweeps shown earlier in Fig. 8 identified that the lift coefficient of the ice shells was more sensitive to changes in Reynolds number compared to the results in turbulent flow. The drag and lift coefficients for Model S2-B in turbulent and smooth flow are compared in Fig. 14a for three pitch angles of 0°, 10°, and 30°. The results for Model S9-Sim in turbulent and smooth flow are compared in Fig. 14b at the same pitch angles. The results show that the ice shell with the smoother outer surface (S2-B) is affected by the flow regime more than Model S9-Sim, which has a textured outer surface composed of simulated ice. This difference is apparent in the lift coefficients of Model S2-B at lower pitch angles. At a pitch angle below $\theta = 30°$ the flow is travelling over the curved surface of the ice shell and, therefore, turbulence can greatly affect the location of flow separation. This would affect the magnitude of the aerodynamic forces and moments. However, the outer surface of Model S9-Sim is textured with simulated ice, and the flow separation behaviour is likely dictated by the surface roughness rather than by the flow regime. As a result, the variation of forces

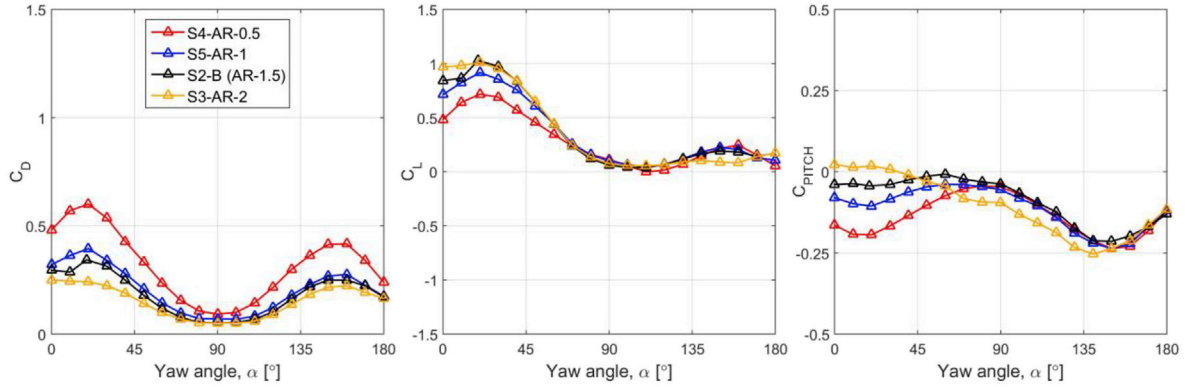

(a) Pitch angle θ = 10°.

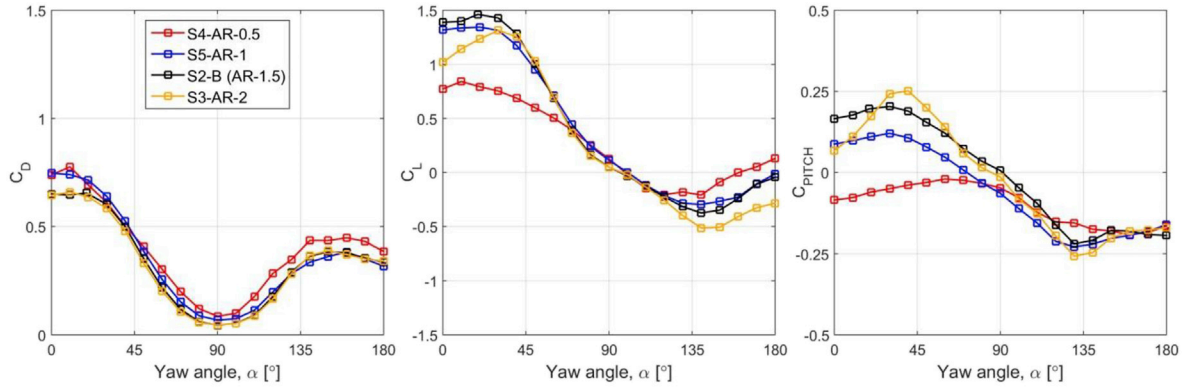

(b) Pitch angle θ = 30°.

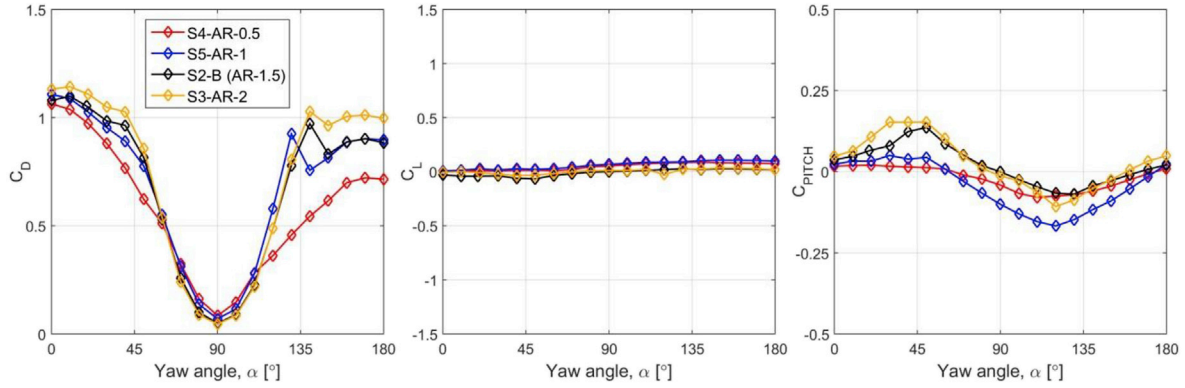

(c) Pitch angle θ = 90°.

Fig. 10. Effect of aspect ratio in turbulent flow. From left to right: drag force coefficient, lift force coefficient, pitching moment coefficient.

between turbulent and smooth flow is much smaller than what had been observed for Model S2-B.

4. Conclusions

This manuscript described the results of a wind tunnel test of generic, representative ice shell models tested in the NRC 1.0 m × 0.8 m Pilot Wind Tunnel. The objective of the study was to measure aerodynamic forces and moments of the ice shells to be used in a 6-DOF numerical model for simulating the trajectory of ice falling from the inclined cables of cable-stayed bridges and suspension bridges. Nine models were selected for wind tunnel testing to represent different aspect ratios, curvatures, thicknesses, and external surface conditions. All of the models were tested in turbulent flow with a turbulence intensity of 7% and a length scale of 0.05 m. Two of the ice shells were also tested in smooth flow to understand the impact of flow turbulence on the aerodynamic behaviour of the ice shells. The main findings of this study are:

- Due to the sharp edges of the ice shells, the air flow around them can be considered as Reynolds number insensitive in turbulent flow above a Reynolds number of 100,000.
- On a real bridge site, the natural wind is turbulent and the range of Reynolds numbers associated with a falling ice piece will be similar to or greater than the values in the current work. Therefore, it can be assumed that the air flow around a falling ice fragment on real bridge site will likely be Reynolds number insensitive. As a result, the aerodynamic coefficients for an ice trajectory model can be considered as a function of the relative orientation between the ice shell and the wind vector, and not as a function of the wind speed.

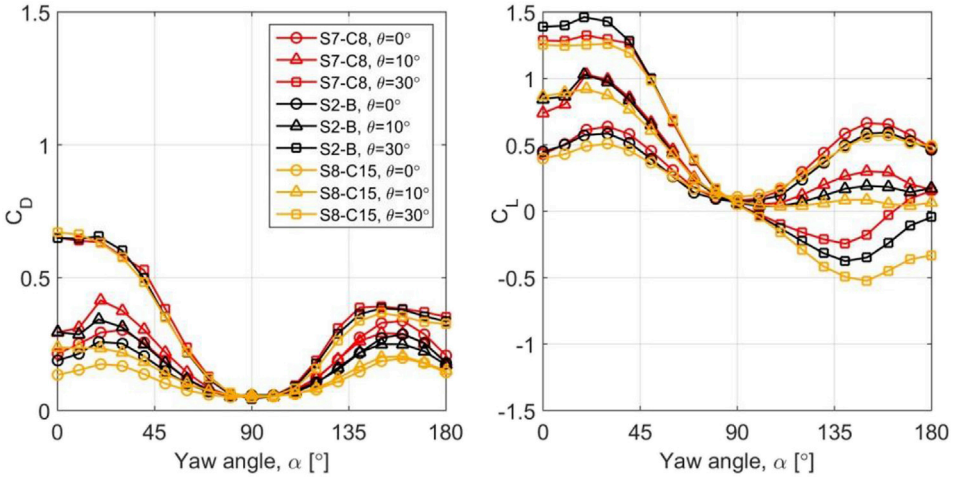

Fig. 11. Effect of ice-piece curvature at several pitch angles in turbulent flow. Left subfigure: drag force coefficient as function of yaw angle, Right subfigure: lift force coefficient as function of yaw angle.

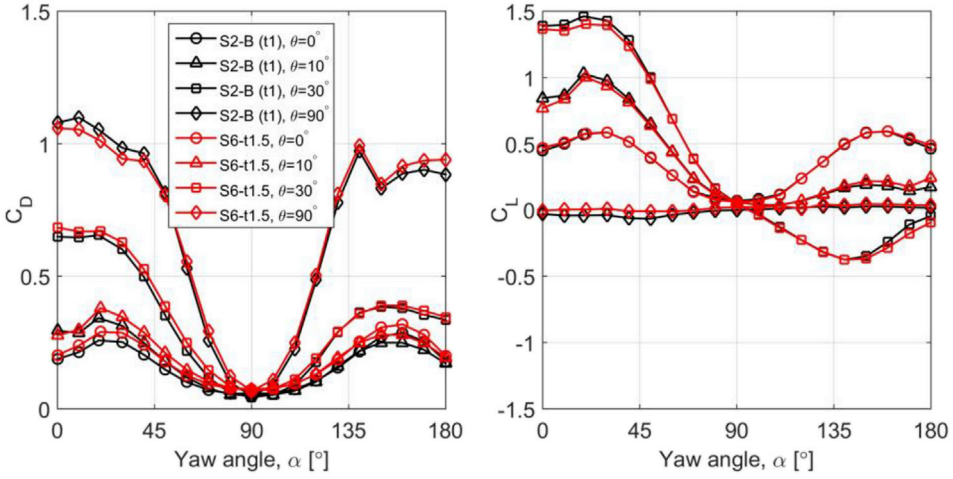

Fig. 12. Effect of ice-piece thickness at several pitch angles in turbulent flow. Left subfigure: drag force coefficient as function of yaw angle, right subfigure: Lift force coefficient as function of yaw angle.

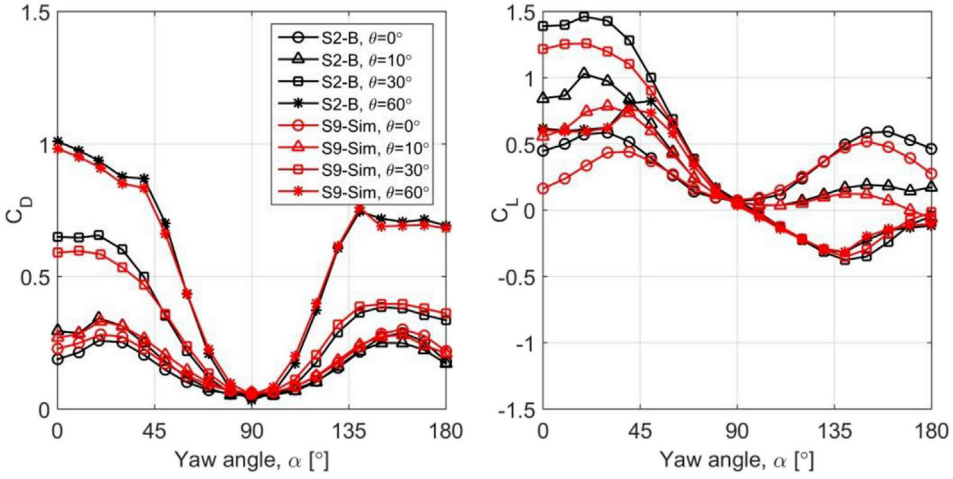

Fig. 13. Effect of ice surface conditions at several pitch angles in turbulent flow. Left subfigure: drag force coefficient as function of yaw angle, Right subfigure: lift force coefficient as function of yaw angle.

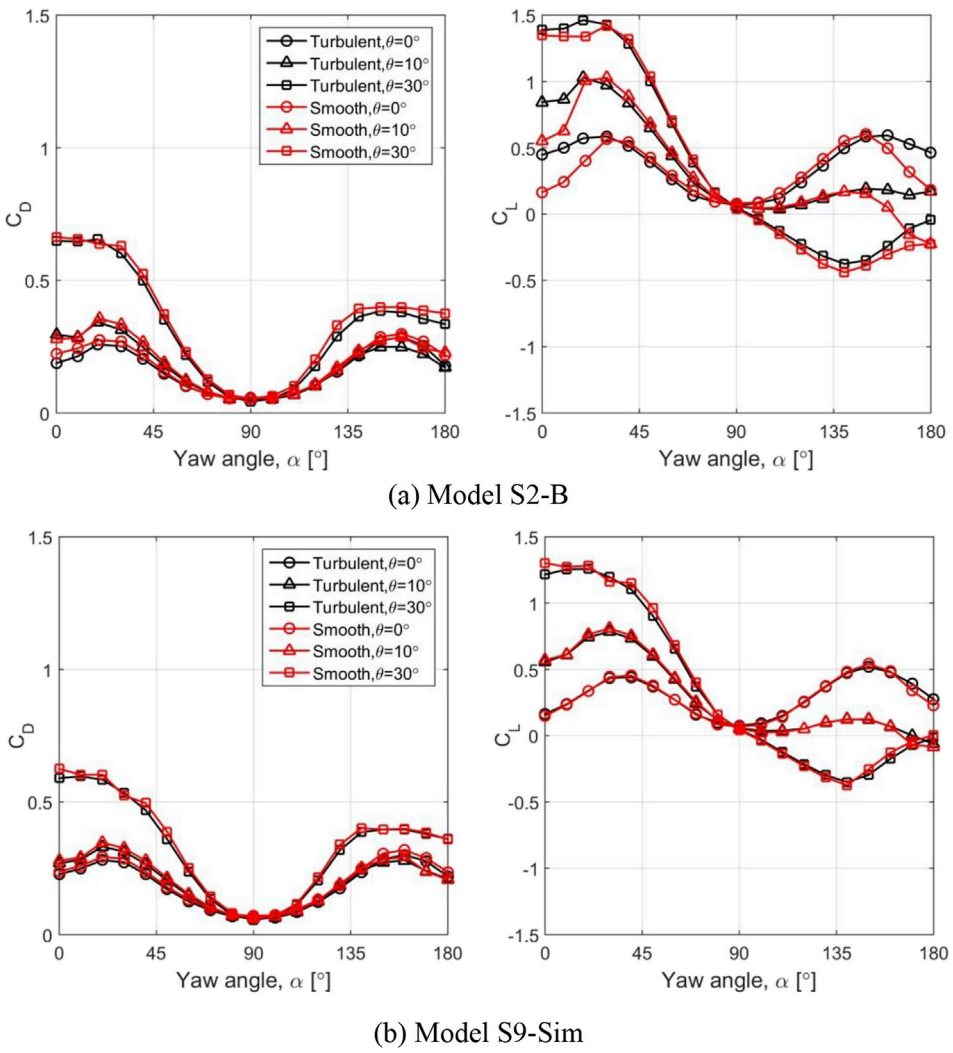

Fig. 14. Effect of turbulence on at several pitch angles. Left subfigure: drag force coefficient as function of yaw angle, Right subfigure: lift force coefficient as function of yaw angle.

- The presence of curvature on a model leads to a significant difference in drag, lift, and pitch coefficients, when compared to a flat plate with the same aspect ratio.
- Of the three geometrical factors that define the ice shells, the aspect ratio had the most effect on the aerodynamic force and moment coefficients based on the results for model geometries that were considered. The ice shell curvature had a smaller effect on the aerodynamics while the thickness of the models did not have a significant effect.
- The effect of a simulated ice surface and of flow turbulence are similar. It is assumed that the textured surface of the ice shell with simulated ice accretion and the effect of flow turbulence both modify the aerodynamic behaviour of the ice shell at lower pitch angles by altering the location of flow separation on the model.

Future work to incorporate the aerodynamic force and moment coefficients into a 6-DOF trajectory model is underway with the goal of developing higher-fidelity bridge monitoring tools.

Acknowledgements

The current work was funded by Infrastructure Canada as part of the Climate-Resilient Buildings and Core Public Infrastructure project. The authors would like to thank the technical support team in the NRC Aerodynamics Laboratory for their assistance.

References

Baker, C., 2007. The debris flight equations. J. Wind Eng. Ind. Aerod. 95, 329–353.
Biswas, S., Taylor, P., Salmon, J., 2012. A model of ice throw trajectories from wind turbines. Wind Energy 15, 889–901.
Canadian Consulting Engineer, 2013. Engineers Offer Solutions to Ice Problems on Portmann Ridge. URL: https://www.canadianconsultingengineer.com/transportation/engineers- offer-solutions-to-ice-problems-n-port-mann bridge/1002007259/.
Canadian Standards Association, 2010. CAN/CSA-C22. 3 No. 60826-10 Design Criteria of Overhead Transmission Lines. Canadian Standards Association, Mississauga.
Cheng, C., Auld, H., Klaassen, J., Li, Q., 2007. Possible impacts of climate change on freezing rain in south-central Canada using downscaled future climate scenarios. Nat. Hazards Earth Syst. Sci. 7, 71–87.
Cheng, C., Li, G., Auld, H., 2011. Possible impacts of climate change on freezing rain using downscaled future climate scenarios: updated for eastern Canada. Atmos.-Ocean 49 (1), 8–21.
Fu, A., Huang, P., Gu, M., 2013. Numerical model of three-dimensional motion of plate-type wind-borne debris based on quaternions and its improvement in unsteady flow. Appl. Mech. Mater. 405, 2399–2408.
Grayson, M., Pang, W., Schiff, S., 2012. Three-dimensional probabilistic wind- borne debris trajectory model for building envelope impact risk assessment. J. Wind Eng. Ind. Aerod. 102, 22–35.
Holmes, J., 2004. Trajectories of spheres in strong winds with application to wind-borne debris. J. Wind Eng. Ind. Aerod. 92, 9–22.

Holmes, J., Letchford, C., Lin, N., 2006. Investigations of plate-type wind- borne debrispart ii: computed trajectories. J. Wind Eng. Ind. Aerod. 94 (1), 21–39.
Martinez-Vazquez, P., Baker, C., Sterling, M., Quinn, A., 2009. The flight of wind borne debris: an experimental, analytical, and numerical investigation. Part I (Analytical Model). In: Proc. Of 5th European and African Conference on Wind Engineering (EACWE5).
Neron, J.-F., 2017. Opération déglaçage sur le pont Laporte (in french). URL: https://www.lesoleil.com/actualite/operation-deglacage-sur-le-pont- laporte-1d54c8955e044d1e085204e79f599d1a.
Ng, J., 2012. Photos: the Port Mann and Other Cable- Stayed Bridges Around the World with Ice Issues. URL: http://www.vancouversun.com/news/7727913/story.html?tab=PHOT.
Noda, M., Nagao, F., 2010. Simulation of 6DOF motion of 3D flying debris. In: Proc. Of Fifth International Symposium on Computational Wind Engineering (CWE2010).
Renström, J., 2015. Model of Ice Throws from Wind Turbines. Tech. Rep. Uppsala University.
Richards, P., 2010. Steady aerodynamics of rod and plate type debris. In: Proc. Of 17th Australasian Fluid Mechanics Conference.
Richards, P., Williams, N., Laing, B., McCarty, M., Pond, M., 2008. Numerical calculation of the three-dimensional motion of wind-borne debris. J. Wind Eng. Ind. Aerod. 96, 2188–2202.
Structural Engineering Institute, 2010. Minimum Design Loads for Buildings and Other Structures, vol. 7. Amer Society of Civil Engineers.
Szilder, K., 2017. Numerical modeling of ice accretion shape due to freezing precipitation of engineering structures. In: Proc. Of the European-african Conference on Wind Engineering (EACWE2017). No. 64.
Szilder, K., 2018. Theoretical and Experimental Study of Ice Accretion Due to Freezing Rain on an Inclined Cylinder. Cold Regions Science and Technology In Press (in press).